LA-UR-   11-00238

Title: Lift, Drag and Flow-Field Measurements around a Small Ornithopter

Author(s):   Ramiro Chavez-Alarcon, Fangjun Shu, B.J. Balakumar

Los Alamos
NATIONAL LABORATORY
——— EST.1943 ———

Form 836 (7/06)

Lift, Drag and Flow-field Measurements around a Small Ornithopter

Ramiro Chavez-Alarcon* and Fangjun Shu†

Mechanical & Aerospace Engineering Department, New Mexico State University, Las Cruces NM, USA

B. J. Balakumar‡§

Physics Department, Los Alamos National Laboratory, Los Alamos NM, USA

The aerodynamics of a flight-worthy, radio controlled ornithopter is investigated using a combination of Particle-Image Velocimetry (PIV), load cell measurements, and high-speed photography of smoke visualizations. The lift and thrust forces of the ornithopter are measured at various flow speeds, flapping frequencies and angles of attack to characterize the flight performance. These direct force measurements are then compared with forces estimated using control volume analysis on PIV data. High-speed photography of smoke streaks is used to visualize the evolution of leading edge vortices, and to qualitatively infer the effect of wing deformation on the net downwash. Vortical structures in the wake are compared to previous studies on root flapping, and direct measurements of flapping efficiency are used to argue that the current ornithopter operates sub-optimally in converting the input energy into propulsive work.

Nomenclature

U   Horizontal velocity component
V   Vertical velocity component
St   Strouhal number
Re   Reynolds number based on free-stream speed and chord length
D   Drag
c   Chord length
s   Wingspan
T   Thrust
V   Voltage
I   Current
η Efficiency
α Angle of attack
f   Flapping frequency
A   Flapping amplitude

I. Introduction

The high maneuverability and aerodynamic benefits of biological fliers offer tantalizing design guidelines for the construction of robotic flapping wing micro-air vehicles. Nature's fliers obtain such flight characteristics by a combination of complicated wing motions (such as flapping, twisting and folding) and have flexible wings that results in a modification of camber and a varying angle of attack along the wing span during the entire stroke.[1] Although experimental and computational studies of different flapping mechanisms have

---

American Institute of Aeronautics and Astronautics

provided useful aerodynamic information, the flow physics is still not yet fully understood, mainly due to the difficulties of measuring the complex three-dimensional and transient fluid dynamics associated with flapping flight.

Wake structures and their relationship to propulsive efficiency have been widely investigated for airfoils and panels with flapping motions such as heaving, pitching and plunging (see Godoy-Diana et al.[2] for example). A critical parameter that determines the wake structure (and hence the propulsive efficiency) is the Strouhal number:

$$St = \frac{fA}{U} \tag{1}$$

where f is the flapping frequency, A is the wake width (or flapping amplitude), and U is the free-stream velocity. One motivation for these studies is to better understand the aerodynamic mechanisms used by birds and swimmers for propulsion, and apply this knowledge to design efficient flying and swimming robots. In particular, it is interesting to note that the propulsive efficiencies of various swimming animals like dolphins, sharks and bony fish reach their peaks at a narrow Strouhal number range of $0.2 < St < 0.4$.[3]

Godoy-Diana et al.[2] performed a PIV study of the quasi-2D mechanism of the near wake of a pitching airfoil. The study showed that propulsive wakes were generated at a specific region in the flapping frequency–amplitude space. In these regions, the sign of each vortex in the Benard-von Karman wake was flipped to indicate propulsion instead of drag. These reversed Benard-von karman wakes have been observed in the wake of swimming animals. In order to determine the effect of wing compliance on the aerodynamic forces, Heathcote and Gursul[4] performed experiments on flexible, plunging airfoils with constant amplitude and varying the Reynolds numbers up to 27000. Measurements of the thrust and momentum flux coefficients for different airfoil stiffness showed a peak at particular values of plate thickness indicating the importance of wing flexibility on optimal thrust generation. Epps et al.[5] performed wake studies to characterize the performance of fish-like swimming robots at Reynolds and Strouhal numbers of 7500 and 0.86 respectively. During nominal swimming, these robots produced two reverse Benard-von Karman streets in a V-shaped wake. The thrust generated by the robots was calculated from high speed PIV measurements that were found to be in agreement with static measurements from a load cell attached to the model.

While swimming is an oft-studied form of propulsion, root flapping motion, which is the wing motion corresponding mostly to flying animals like birds and insects has received much less attention. A notable difference in root flapping experiments is the presence of three-dimensional effects that are difficult to study experimentally. Vest and Katz[6] performed experiments to validate an unsteady numerical method capable of modeling root flapping motion in variable geometry wings. Using a six-component load balance, the experimental measurements were observed to show agreement with the aerodynamic forces estimated by numerical analyses. Wind tunnel studies by Lin et al.[7] measured the lift and thrust of flexible wings under various flapping frequencies, free-stream velocities and angles of attack. The wings were constructed of epoxy reinforced carbon fiber frames covered with PVC plastic films. At high flapping frequencies, it was shown that the aerodynamic forces were affected by the flexibility of the wings. Also, a positive angle of attack was found necessary for the wings to generate lift.

Spedding et al.[8] flew a live bird (Thrush Nightingale) in a low turbulence wind tunnel and measured the wake structures using 2D PIV. While traditionally, bird wakes were understood to fall into one of the two standard cases consisting of closed loop discrete vortex model at low flight speeds, and constant circulation continuous vortex model at medium to high speeds, Spedding et al.'s measurements showed an intermediate structure. Calculations showed that all of the measured wake structures had enough momentum to provide weight support over the wing beat. Around the same time, an investigation of flying and swimming animals by Taylor et al.[3] has shown that root flapping animals (flying animals), like swimming fish, also fall in the Strouhal number range where the efficiency is high, but only while cruising. According to this investigation, experiments with heaving or pitching airfoils have shown efficiencies of 70% and 80% when the Strouhal number is between 0.2 and 0.4.

The present investigation attempts to build upon the previous experiments to characterize the aerodynamics of a robotic ornithopter using a combination of load cell measurements, flow visualization, PIV and high speed camera diagnostics. In the current experiments, the toy ornithopter operates at a Reynolds number of $Re = 8322$ (based on the free-stream velocity and the wing chord) and a Strouhal number of $St = 0.8$. Load cell measurements provide lift and thrust variations over a parameter space formed by varying angles of attack, free-stream velocities and flapping frequencies. Experiments with a high speed camera and a smoke wire helped visualize the flow around the model to obtain useful information about the presence and behavior of leading edge vortices. In addition, the three dimensional structure of the wake vortices and their

American Institute of Aeronautics and Astronautics

relationship to the ornithopter's aerodynamic efficiency are also investigated. The effect of free-flight wing deformation in affecting the LEV vortex shedding mechanisms is also captured using time-series photographs. PIV measurements are used to obtain average velocity fields around the model to measure the thrust and lift distributions along the wingspan.

II.   Experimental Setup

All the measurements, except the recordings of the ornithopter in free-flight, were performed at the low-turbulence, open return wind tunnel facility at New Mexico State University using a six-axis load cell, Particle Image Velocimetry, high speed video cameras and smoke wire visualization diagnostics. The test section of the wind tunnel has a cross-section of 1.3 m×1.2 m and is 14.6 m in length. Although the tunnel has a maximum free-stream velocity of 35 m/s, most of the measurements were performed at 1-2 m/s, near the free-flight speed of the ornithopter. All the measurements around the ornithopter were performed under laminar inflow conditions, with a measured free-stream turbulence intensity of less than 2%.

(a) Ornithopter
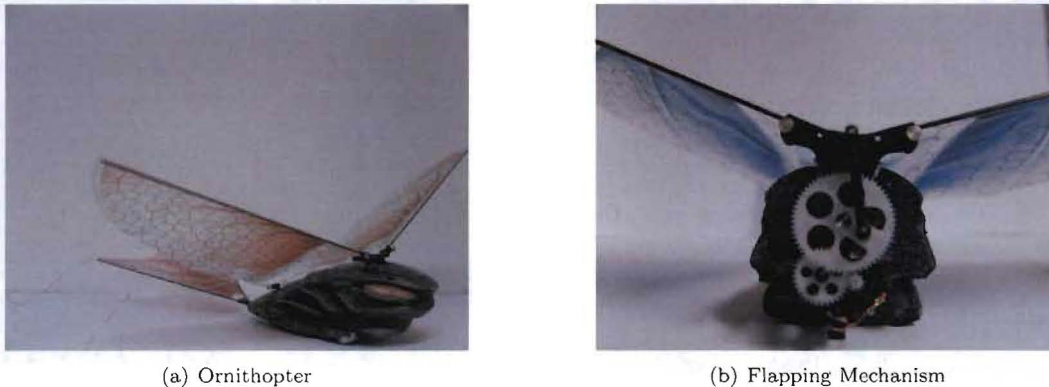

(b) Flapping Mechanism

Figure 1. (a) Photograph of the ornithopter (i-Fly Vamp by Interactive toy concepts) used for the present experiments. (b) The gear-crank flapping mechanism used to convert the rotary motion of the motor to flapping motion of the wings.

II.A.   Ornithopter Specifications

Several ornithopter models are available in the market over a range of sizes. After experimenting with many of these models, we decided to perform our experiments on an *i-vamp* radio-controlled ornithopter manufactured by Interactive Toy Concepts due to its flight characteristics including stability, ease of control and robustness (Fig. 1(a)). Further these ornithopters are easily available and their parts could be readily replaced. The current experiments were performed on an ornithopter that weighs 11.3g in flight (including battery). The ornithopter has a length of 0.2m and a wingtip-wingtip span of 0.3m. The nominal angle of attack on the wings and the flapping angle were measured to be 13.4° and 40° respectively.

The free-flight speed of the ornithopter was measured using several time-of-flight techniques including a high-speed camera, measurements between laser markers and using visual measurements. While small variations were measured between these methods, primarily due to the difficulties involving the maintenance of a steady flight during the experimental duration, the average speed was measured to be 1.7 m/s. At this speed, the corresponding flapping frequency of the ornithopter was measured to be 16.6 Hz using light interruptions from a laser pointer as measured using a photo diode.

The flapping frequency of the ornithopter is controlled by modulating the supply voltage to the direct current motor that drives the flapping mechanism. During wind tunnel tests, the battery inside the ornithopter was disconnected and replaced by a regulated precision external power source to eliminate flapping frequency variations during the experiment. The flapping motion of the ornithopter is symmetric, and is generated from the rotary motion of the motor shaft using a gear-crank mechanism shown in Fig. 1(b). The shape of each wing is closely approximated by a quarter ellipse with a wing span (semi-major axis) of 0.136 m and a maximum chord length (semi-minor axis) of 0.082 m. The pliant but inelastic wings of the ornithopter are made up of an unknown polyurethane-like material and are mounted to a flexible rod at its leading edge. The trailing edge of each wing is attached to a connected set of pivots, whose angular variations translate to

American Institute of Aeronautics and Astronautics

turning motions of the ornithopter. The tail of the ornithopter resembles a delta wing and is mounted at a negative angle of attack of 18.6° with the wider edge of the wing at its trailing edge. A vertical plastic keel is attached to the tail, presumably for additional stability.

The free-stream Reynolds number (based on the free-stream velocity and the wing chord) was measured to be 8322 at a Strouhal number of 0.8. The simplicity of the ornithopter's design and the relatively ease with which its aerodynamics could be characterized (unlike birds) make it an attractive target for 3D numerical simulations.
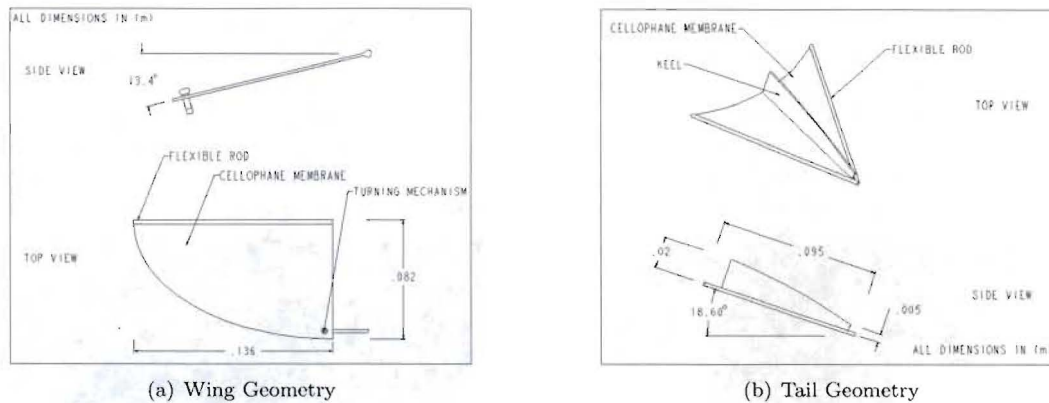

(a) Wing Geometry

(b) Tail Geometry

Figure 2. Parts schematic and corresponding dimensions of the ornithopter's flexible wing and tail.

II.B.   Particle Image Velocimetry

One of the principal difficulties of using PIV to perform high-resolution measurements of the flow around ornithopters (and birds) is the necessity of moving the camera in a systematic manner around the flow field without undue changes in the magnification. This problem was overcome in the present experiments by mounting both the laser and the camera on a heavy-duty triple-axis translation stage (Velmex Bislide) equipped with stepper motors and controllers (Fig. 3(a)). The translation stage had a resolution of 0.00025 in per step in the X-, Y-, and Z- directions. The laser heads and the optics were capable of movement in the X-Z plane while the camera was capable of movement in all three directions (see Fig. 5 for coordinate axes). Such a design was chosen to eliminate the necessity of readjusting the optics due to constraints imposed by the wind tunnel floor on the vertical motion of the optics. A non-intrusive triggering system using a red-laser and a photo-diode system fitted to a high-pass filter (to differentiate the wavelength of the Nd:YAG PIV laser) was used to obtain phase locked PIV measurements (Fig. 4(a) and 4(b)).
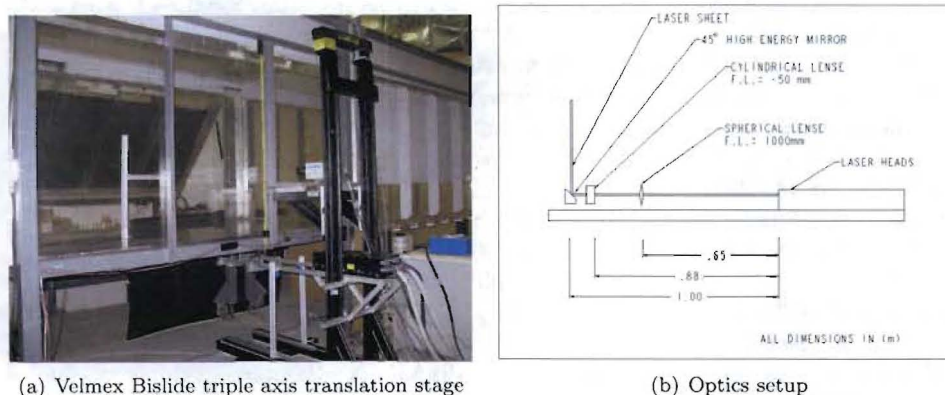

(a) Velmex Bislide triple axis translation stage

(b) Optics setup

Figure 3. (a)Translation stage used to mount lenses, camera and lasers; (b) Optics schematic

The 2D PIV measurements were obtained with the laser light sheet aligned along the streamwise-wall normal direction. The PIV light sheet was generated by a dual-head 532nm Nd:YAG Big Sky laser. The

American Institute of Aeronautics and Astronautics

width (streamwise dimension) of the light sheet varied from 2cm close to the bottom of the wind tunnel to roughly 7.6cm at the top of the test section (Fig. 3(b)). The light-sheet at the waist was measured to be roughly 2mm. A Laskin nozzle seeder was used to generate olive oil seed particles with a mean diameter of approximately $1\mu m$.[9] The seeder was located at the end of the diffuser to ensure a homogeneous distribution of the particles in the facility, and to ensure that the intake of the tunnel remained undisturbed. A Motion Pro X5 plus camera and a timing hub (by IDT, Tallahassee, FL) were used to capture the images of the seeded flow. The size of the PIV grid was 0.041m in width and 0.134m in height. Phase-locked PIV measurements were performed with the ornithopter body positioned parallel to the inflow velocity.

(a) Nd:YAG laser and triggering red laser

(b) Plastic tab attached to crank mechanism cuts red laser beam
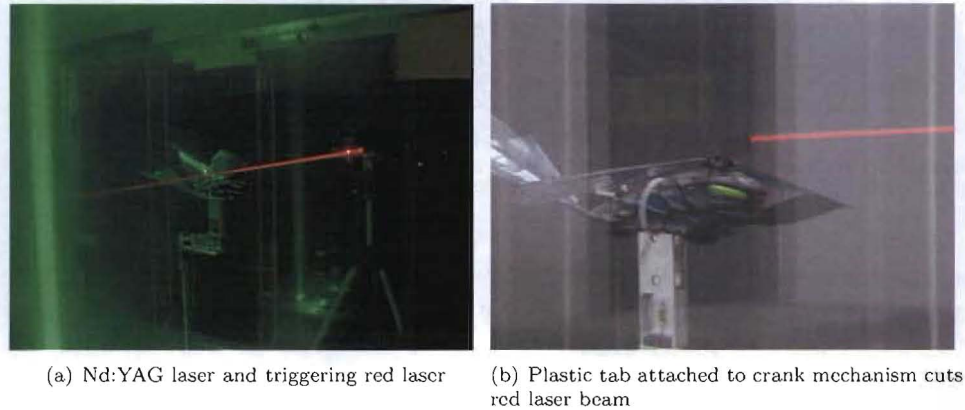
Figure 4. Triggering system

The PIV measurements are used to understand the distribution of the lift and thrust forces along the wingspan. The data presented here were taken during the downstroke when the leading edges were in the horizontal position. The parameters were set to mimic the ornithoper's free flight parameters, i.e. the angle of attack of the ornithopter was 0°, the incoming flow speed was set to the free flight speed (1.7m/s) and the flapping frequency was set to 16.6 Hz. In order to acquire the aerodynamic force distributions along the wing span, the measurements were made at three spanwise locations as shown in Fig. 5. For the PIV experiment, the tail of the ornithopter was removed since it interfered with the laser sheet during the data acquisition process.
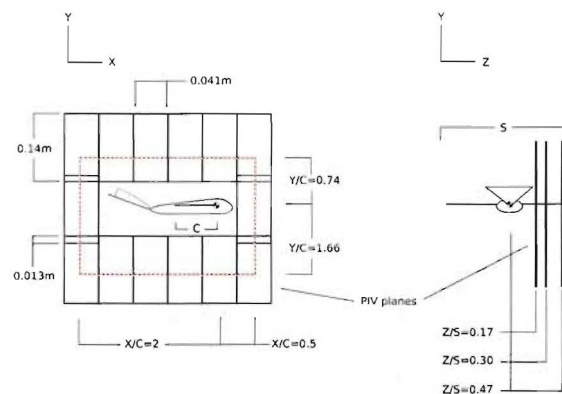

Figure 5. PIV measurement planes. The origin of the coordinate system is located at the intersection of the leading edge with the center line of the body. The red rectangle represents the control volume used the momentum flux analysis.

II.C. Force Sensor Measurements

A 6-axis Nano 17 load cell (ATI industrial automation) with a resolution of 1/320 N, was used to measure the aerodynamic forces generated by the model. The force sensor is cylindrical in shape, with a diameter and length of 2.01 cm and 2.22 cm respectively. The ornithopter was attached to the load cell through a base plate and a hinge to enable an adjustable angle of attack setting (Fig. 6).

American Institute of Aeronautics and Astronautics

Figure 6. Force sensor mounting brackets. This image illustrates how the base plate can be rotated to obtain various angles of attack.

Data was collected at 3000 Hz with a 16-bit 250 KS/s NI PCI-6220 M Series DAQ card. For the test the body of the ornithopter was positioned at angles of attack of 0°, 10°, 20°, 30° and 40°. For each angle of attack, data was obtained at 1.4, 1.7, 2.0, 2.3 and 2.6 m/s and at flapping frequencies of 9.61, 11.61, 13.44, 16.66 and 17.56 Hz.

Prior to every test, a reference value was obtained by averaging 5 s of data while the free-stream velocity was constant and the model was not flapping. Data was recorded for a subsequent 10 s duration at the same speed and while the ornithopter was flapping. The total lift and drag (thrust) was then calculated by subtracting the reference value from the averaged recorded measurement. It was also verified that the mentioned reference values were minimally affected by the phase (flapping) angle of the wings. Tests performed at a free-stream speed of 2.6 m/s and an angle of attack (α) of 0° and 40° showed a variation in the aerodynamic forces of less than 3.5% for the maximum and minimum phase angles, as shown in Table 1.

Table 1. Reference force variation (in Newtons) with phase angle.

	Max. phase angle	Min. phase angle	Variation
Lift: $\alpha = 40°$	-0.8331	-0.8149	2.2%
Drag: $\alpha = 40°$	0.8398	0.8690	3.3%
Lift: $\alpha = 0°$	-0.8766	-0.8669	1.1%
Drag: $\alpha = 0°$	0.7607	0.7372	3.2%

II.D. Smoke-wire and Free-flight Visualization

A high speed camera (Casio Exilim EX-F1 6MP) with maximum fame rate of 1200 fps was used to capture the wing deformation and flow patterns in smoke visualization. The purpose of the smoke visualization was to locate important areas of the wake structure for PIV experiments and to compare the wake structures generated by the flexible wings of the ornithopter to those observed by Taylor[3] in an experiment with a hinged flat plate. A vertical sheet of smoke was generated by an electrically heated wire coated with mineral oil. The wire was placed 1.65 m upstream of the model and smoke sheet was 6.5 cm from the wing tip. The body of the ornithopter was positioned at angles of attack of 0° and 20°. For each angle of attack videos were recorded at 1.2, 1.4, 1.6, 1.7, 1.8 and 2.0 m/s. The flapping frequency was set to 9.61, 13.44 and 16.66 Hz for each case. An additional test for the case of 0° and 1.4 m/s was performed at 7.8 Hz (corresponds to a Strouhal number, St=0.46).

All the free flight visualizations were performed outside of the wind tunnel, due to the challenges in flying a bird in free flight inside the wind tunnel. The high-speed camera was placed facing a gridded cardboard and the model flew between the camera and the grid. The video was then analyzed to acquire free flight speed, flapping frequency and also to observe the changing in angles of attack and deformation of the wings.

American Institute of Aeronautics and Astronautics

III. Results

III.A. Lift and thrust force variations with angle of attack, mean velocity and flapping frequency

The variation of the net lift and thrust forces generated by the flapping wings is shown in Fig. 7 and 8 for various flight velocities and for various angles of attack. The measurements represent only the lift and thrust generated by the flapping wings, i.e., aerodynamic forces generated by the body of the model and the mounting brackets are subtracted. It is clear that for all the cases, an increase in the flapping frequency results in an increase in the lift force even at high angles of attack. While this might be advantageous at first sight, this enhanced lift is accompanied by an increase in the drag force also. Thus, merely increasing the flapping frequency of an ornithopter to generate enhanced lift is insufficient from a design perspective. This increase must also be accompanied by a larger power source for a given duration of flight and power density.

At each flapping frequency, an increase in the mean velocity results in a decrease in the net thrust force. For certain combinations of the (flapping frequency, mean velocity, angle of attack) triplets, the net thrust force generated by the wing exactly equals the drag on the ornithopter (Fig. 8). At these flight parameters, the bird might be expected to fly in a steady flight pattern. Thus, the parametrization of the lift and drag forces for various mean velocity, angle of attack and flapping frequencies combinations is a critical first step in understanding ornithopter flight. Moreover, such data also allow the validation of numerical simulations under various physical regimes (e.g. separated flow around wings) without accounting for the motion of the ornithopter as a whole.

It is also clear from an examination of the curves that the sensitivity of the lift and thrust forces to changes in the angle of attack are different. While the lift forces are most sensitive to small changes in the angle of attack for small angles of attack, the thrust forces are most sensitive for large angles of attack. Since the free-flight angle of attack was measured to be less than 20°, it can be expected that small changes to the ornithopter's angle of attack will have a larger impact on the lift forces than they would on the thrust.

III.B. Distribution of aerodynamic forces along wing span and control volume analysis of PIV measurements

Since load-cell measurements only provide the integrated forces generated by the wings, PIV experiments were conducted to analyze the distribution of the aerodynamic forces along the wingspan. The profiles of the vertical and horizontal velocity components corresponding to the incoming and wake flow in the three spanwise measurements planes are shown in Fig. 9 - 10. In the wake, an increase in the horizontal velocity is observed at the wingspan sections $Z/S = 0.17$ and $Z/S = 0.30$, indicating the generation of propulsive thrust by the inboard region of the wing. On the other hand, horizontal velocity deficit is observed in the $Z/S = 0.47$ plane (over $-2 < Y/C < -0.5$) corresponding to a drag force on the outboard edge of the wing. The results suggest that thrust is mainly generated by the wing sections close to ornithopter's body. Similar trends were observed for the vertical velocity in the wake (Fig. 10), i.e., greater downwash in the $Z/S = 0.17$ and $Z/S = 0.30$ plane, corresponding to lift generation in the inboard region of the flapping wing.

A velocity surplus corresponding to the incoming horizontal and vertical component is observed in Fig. 9. This induced velocity is commonly observed in velocity measurements on control surfaces drawn close to the leading edge of a lift-producing wing. PIV measurements (not presented here) on surfaces taken far away from the leading edge show nominally flat inflow velocity profiles without the velocity surplus observed here. The observed velocity surplus is caused by the induction generated by the circulation present around the airfoils. This circulation (and hence the induced velocity) is caused by both the bound vorticity around the airfoil and by the vorticity carried by the leading edge vortices. The ensuing curvature of the streaklines near the leading edge of the flapping wing due to the presence of wing circulation is also observed in the smoke flow visualizations presented in the next section.

To facilitate a control volume analysis on a closed surface, velocity measurements were also performed on the top and bottom measurement locations and are shown in Fig. 11 - 12. The plots corresponding to the top and bottom vertical components show a maximum velocity surplus at $Z/S = 0.30$ followed by the section $Z/S = 0.17$ and then the section $Z/S = 0.47$. For the bottom horizontal velocity components, the distribution is similar, except that in this case a clear velocity deficit is observed in the range $-2 < X/C < -0.75$.
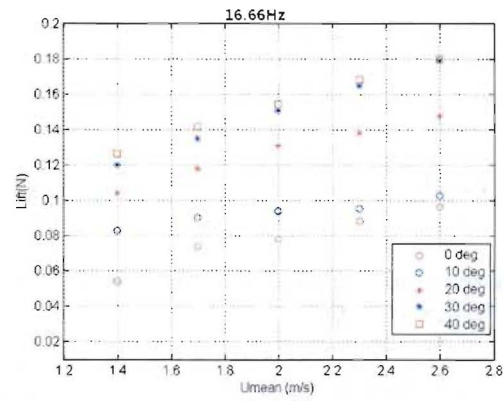
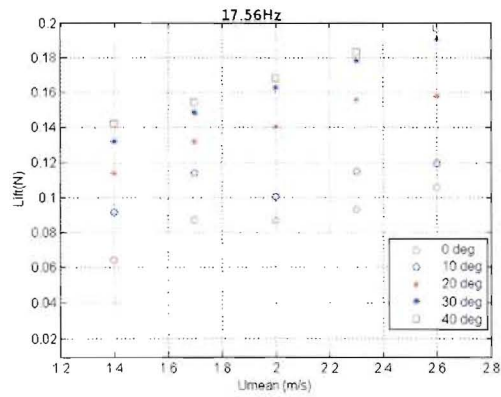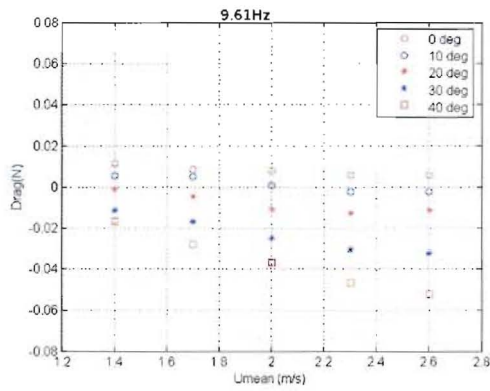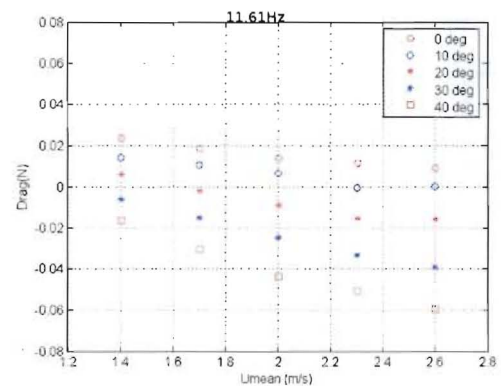American Institute of Aeronautics and Astronautics
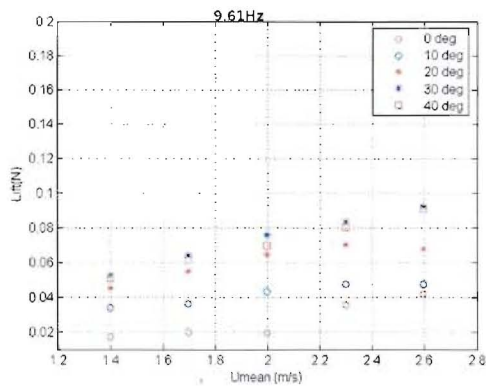
(a)
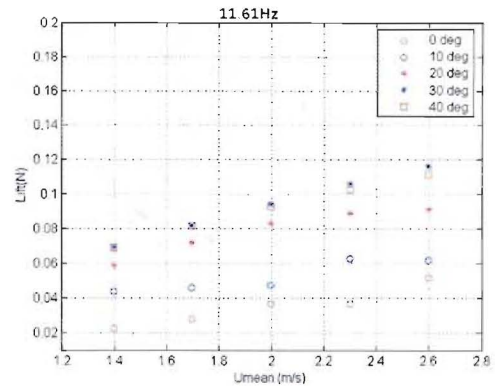
(b)
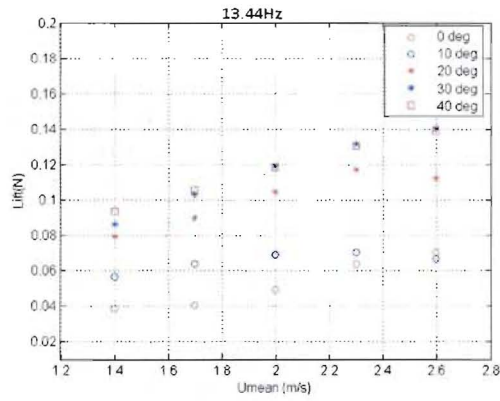
(c)

(d)

(e)

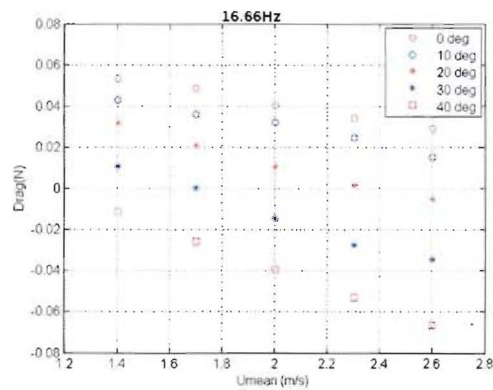Figure 7. Lift vs Umean, all flapping frequencies

American Institute of Aeronautics and Astronautics

(a)

(b)
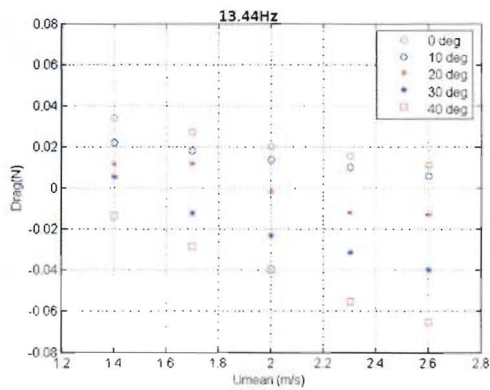
(c)

(d)
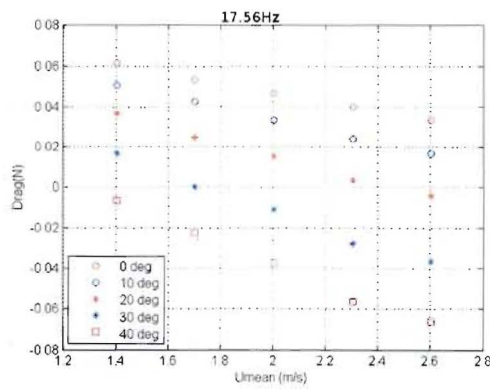
(e)

Figure 8. Drag vs Umean. Drive voltage: 2.0-4.2V

American Institute of Aeronautics and Astronautics
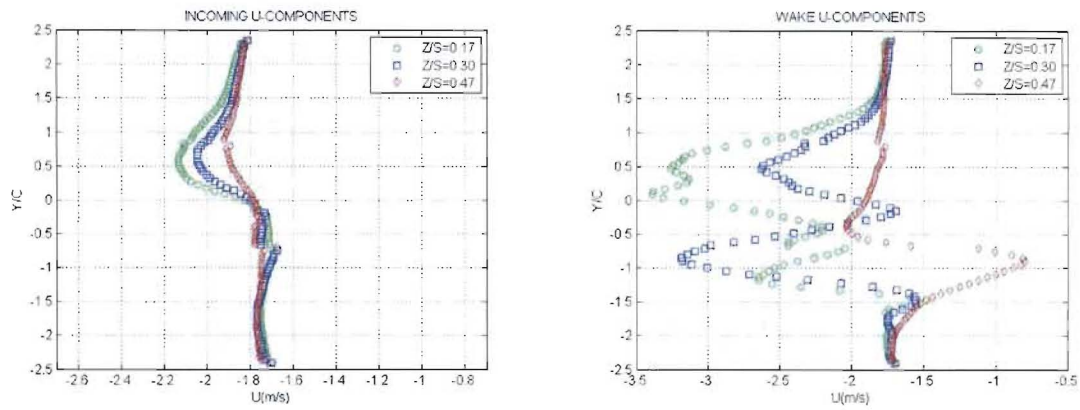
Figure 9. Incoming (left) and wake (right) horizontal velocity component
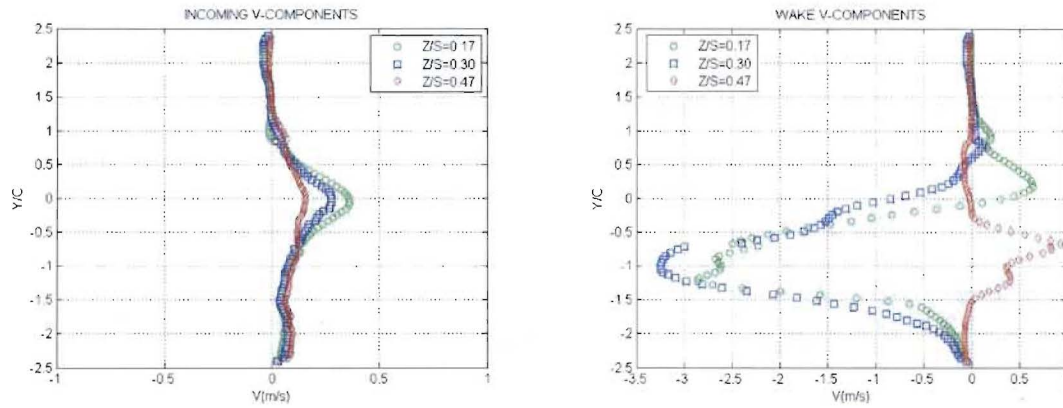

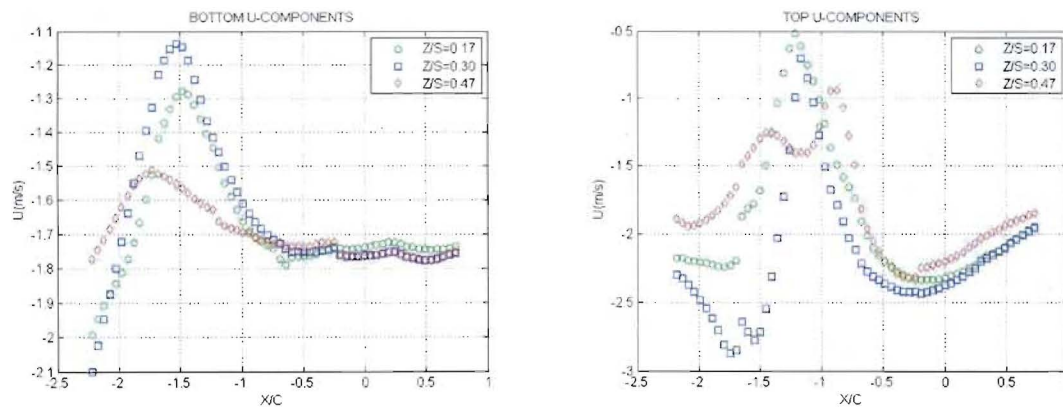Figure 10. Incoming (left) and wake (right) vertical velocity component

Figure 11. Horizontal velocity components of flow through the top (left) and bottom (right) surfaces of the control volume.

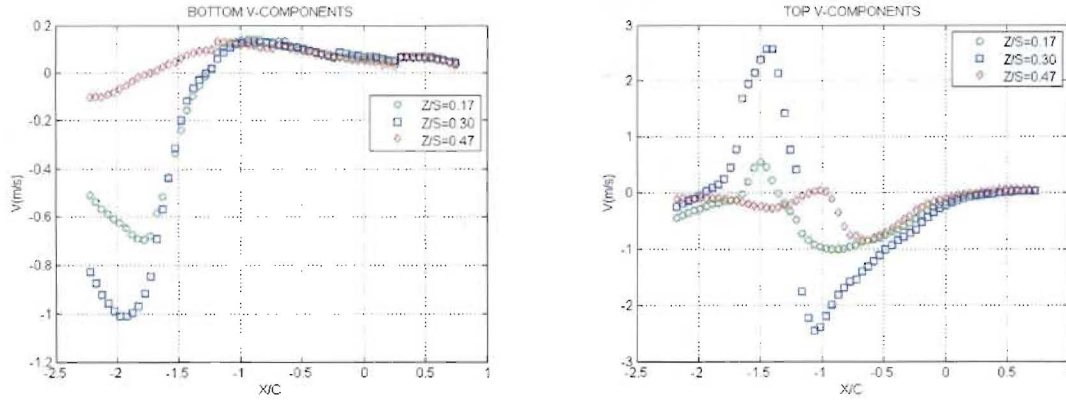American Institute of Aeronautics and Astronautics

Figure 12. Vertical velocity components of flow through the top (left) and bottom (right) surfaces of the control volume.

To estimate the distribution of the aerodynamic forces along the wing span, momentum flux analysis was performed at the planes shown in Fig. 5. Under the assumption of steady flow, the linear momentum shown in Eqn. 2 can be simplified to Eqn. 3.

$$\frac{\partial}{\partial t} \int_{cv} \mathbf{V}\rho \, d\forall + \int_{cs} \mathbf{V}\rho \mathbf{V} \cdot \mathbf{n} \, dA = \sum F \tag{2}$$

$$\int_{cs} \mathbf{V}\rho \mathbf{V} \cdot \mathbf{n} \, dA = \sum F \tag{3}$$

The thrust and lift distributions obtained from Eqn. 3 are shown in Fig. 13. Consistent with our previous arguments, it is seen that the tip region of the wing contributes substantially less to the generation of lift and thrust forces.

The total aerodynamic thrust and lift forces generated by the ornithopter are estimated from PIV measurements by integrating the curves in Fig. 13 to be 0.049 N and 0.060 N respectively (after accounting for the forces acting on both wings). The force sensor measurements indicate that at these flight parameters the thrust and lift are approximately 0.05 N and 0.075 N respectively. The deviations from the force sensor measurements are 2% and 20% for the thrust and lift respectively. It is helpful to discuss the causes for the deviation of the lift force estimates between the load cell and PIV measurements. Firstly, the integration of the lift forces measured using PIV are performed using only 3-points along the curve (Fig. 13). The measured drop in the lift near the wing tip is caused by the tip vortex and is localized in the wing region over a spanwise length of the order of the wing chord. Hence, using more spanwise measurement planes is expected to improve the lift force estimates. On the same token, the thrust force estimates using PIV are also expected to increase, resulting in a larger disagreement with the load-cell measurements. This disagreement is somewhat mitigated by the fact that the current thrust measurements using the load cell do not include the drag due to the ornithopter fixtures. Secondly, the use of 2D PIV measurements create a bias while performing the control volume analysis. This bias can be removed by performing stereo-PIV measurements on a true control volume instead of the 2D control volume analysis presented here. Thirdly, flow unsteadiness and forces generated by the body of the ornithopter are also unaccounted for. A thorough analysis of the aerodynamics of the ornithopter would include these effects.

III.C. Flow and Free Flight Visualization

Smoke visualization was performed at various mean velocities, flapping frequencies and angles of attack with the wire placed approximately at the mid-span location of the wing. Fig. 18 and Fig. 19 show images at the end of the downstroke, extracted from the videos corresponding to mean velocities of 1.2, 1.7 and 2.0m/s. From an examination of the movies, two main characteristics of the flow field are observed. These are the generation of leading edge vortices (LEV) around the wing, and the presence of mushroom-shaped wake structures that dissipate after approximately three chord lengths from the leading edge. In addition, from a structural perspective, an asymmetric deformation of the wing is clearly observed. The flexible

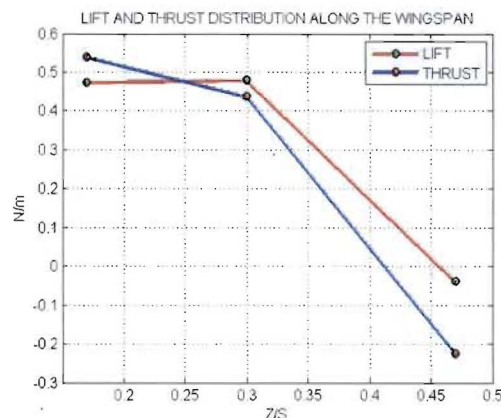American Institute of Aeronautics and Astronautics

Figure 13. Lift and thrust distribution along the wingspan.

wing assumes the shape of a conventional airfoil during the downstroke and an inverted S-shape during the upstroke (Fig. 23).

During the downstroke, a strong LEV along the wingspan is formed and appears to remain attached through most of the stroke. During this time, the incoming streamlines change their direction sharply around the wing and flow over the LEV and the wing, generating a strong momentum sweep in the downward direction. During the downstroke, flow separation does not occur even at high angles of attack. On the contrary, during the upstroke, a much weaker momentum ejection in the upward direction is observed, resulting in a net positive momentum flux in the downward direction to generate a net lift force. While it is not easy to see in the pictures presented here, based on several flow visualization experiments, the LEVs appear to travel along the wingspan during the downstroke. After the completion of the downstroke, the LEVs appear to be shed at the beginning of the upstroke due to a change in the shape of the wing. Similarly, as the wing moves up, a much smaller and weaker LEV appears to be formed on the bottom surface of the wing and is shed at the end of the upstroke (Fig. 17(a) and 17(b)). It should be noted that the LEV during the downstroke is much easier to observe than the LEV present during the upstroke.

Repetitive patterns that look like mushroom shapes are observed in the wake with one pair associated with each stroke cycle. The mushrooms are also associated with one vortex tube structure per wing whose axis of rotation is approximately aligned with the X-Y plane (Fig. 17(b)). The connection between the wing tip vortex and this vortex tube appears unclear from the movies at this point, although we suspect that these two structures are essentially the same. An increase in the mean velocity while keeping the flapping frequency a constant results in a more horizontal vortex tube. The size of the LEV was also observed to be larger for an angle of attack of 20° when compared to 0° (Fig. 18 and 19).

Prominent flow characteristics observed during each cycle of the strokes are illustrated in the schematics shown in Fig. 14 - 16. As shown in Fig. 14, immediately after the downstroke begins, a weak bottom LEV that was formed during the upstroke is shed. Simultaneously, the top LEV begins to form and remains attached to the wing during the entire downstroke. This LEV is associated with a strong downward momentum sweep that causes lift (Fig. 15). The flow during the downstroke also develops a streamwise aligned vortex tube, most likely related to the wing tip vortex that is present in the present finite-span, lift-producing wing (Fig. 16). Finally, at the beginning of the upstroke, the top attached LEV is shed due to a change in the wing shape.

The high quality of the present smoke-flow visualization data motivated a simple linear momentum analysis performed by a visual examination of the video corresponding to the flight parameters of the ornithopter. The trajectories and velocities of small fragments of smoke (located above the wing and in the incoming flow) were determined by extracting a pair of images (Fig. 20) from the flow visualization videos. Since the two images correspond to different times, the distances (in pixels) traveled by these fragments can be measured directly.

Using the known free-stream speed (1.7 m/s), the time difference (δt) between the images and the distance traveled in pixels by the smoke fragment in the incoming flow, the distance (in meters) traveled by the smoke fragment located above the wing was calculated. This distance was then used to determine a flow speed of

American Institute of Aeronautics and Astronautics
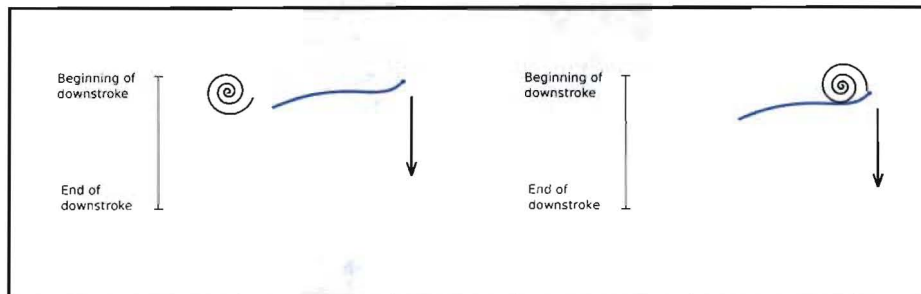
Figure 14. Bottom LEV is shed at the beginning of the downstroke. Top LEV begins to form on the suction side of the wing.
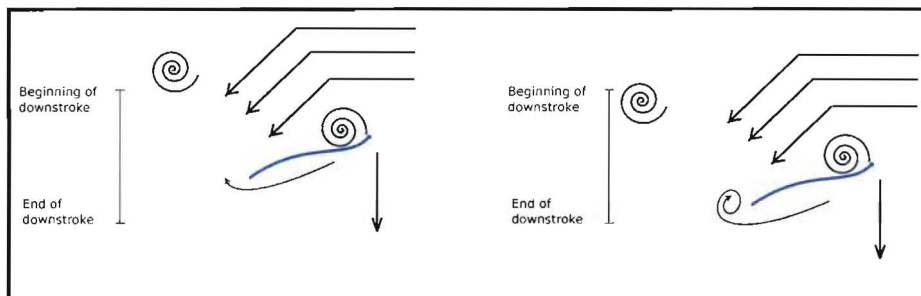

Figure 15. Strong downward momentum sweep associated with the generation of a LEV during the downstroke.
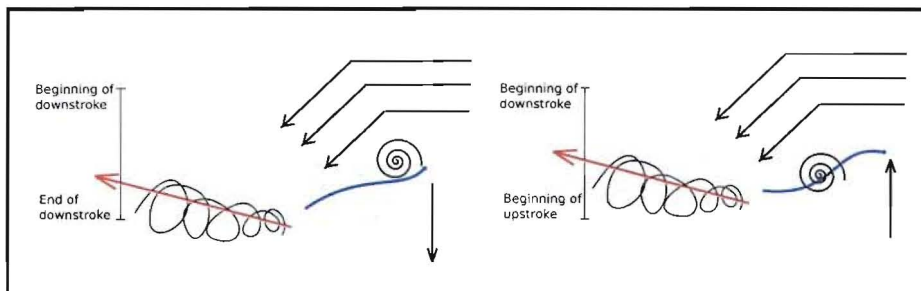

Figure 16. A streamwise vortex is formed due to the difference in pressure on the bottom and top surfaces of the wing. Also at the beginning of the upstroke, the top LEV is shed.

American Institute of Aeronautics and Astronautics

(a) Bottom LEV has been shed

(b) Bottom LEV is still attached to the wing. Vortex tube
is seen below the wing; the red arrow indicates the rotation
of the vortex tube

Figure 17. Vortex tube and bottom LEV shed at the end of the upstroke

2.6 m/s over the wing. The angle of the flow with respect to the X-axis and the area of the inlet and exit were determined to be $\theta = 23.5°$ and 0.007 m^2 respectively. These values were obtained by direct measurement of the pixels in the X and Y directions (Fig. 21). Assuming steady flow and uniform entry and exit velocity distributions of the control volume, the forces exerted by the flow can be calculated by applying a linear momentum equation (Eqn. 2).

Under the assumption of steady flow, the X and Y components of Eqn. 2 become:

$$\int_{cs} U\rho \mathbf{V} \cdot \mathbf{n} \, dA = \sum F_x \tag{4}$$

$$\int_{cs} V\rho \mathbf{V} \cdot \mathbf{n} \, dA = \sum F_y \tag{5}$$

After applying the above equations at the inlet and exit and assuming uniform flow across these boundaries, the integrals reduce to simple multiplications:

$$F_x = V_1^2 \rho A_1 - V_2^2 \rho \cos\theta A_2 \tag{6}$$

$$F_y = -V_2^2 \rho \sin\theta A_2 \tag{7}$$

where $V_1 = 1.7$ m/s, $V_2 = 2.6$ m/s, $\theta = 23.5°$ and $A_1 = A_2 = 0.007$ m^2. Direct substitution of these values in Eqns. 6 and 7 results in a calculated force of $F_x = -0.028$ N and $F_y = -0.024$ N per wing. The force in the X direction (Thrust) seems to be in close agreement with the force sensor measurements, and deviates by 17%. On the other hand, the force in the Y direction (Lift) deviates by 50% from the load cell measurements.

III.D. Efficiency of the ornithopter

The efficiency of the present ornithopter design was examined by comparing the wake structures generated by the ornithopter to those observed by Taylor *et al.*[3] during an experiment with a hinged rigid plate. Smoke-flow visualization images for the flapping ornithopter operating at a Strouhal number of $St = 0.46$ and a Reynold's number of $Re = 6,853$ are shown in Fig. 22. Most interestingly, the wake structures generated by

American Institute of Aeronautics and Astronautics

(a) $1.2m/s$, $16.66Hz$, $St = 1.14$

(b) $1.7m/s$, $16.66Hz$, $St = 0.81$

(c) $2.0m/s$, $16.66Hz$, $St = 0.69$

(d) $1.2m/s$, $13.44Hz$, $St = 0.92$

(e) $1.7m/s$, $13.44Hz$, $St = 0.65$

(f) $2.0m/s$, $13.44Hz$, $St = 0.55$

(g) $1.2m/s$, $9.61Hz$, $St = 0.66$

(h) $1.7m/s$, $9.61Hz$, $St = 0.47$

(i) $2.0m/s$, $9.61Hz$, $St = 0.40$
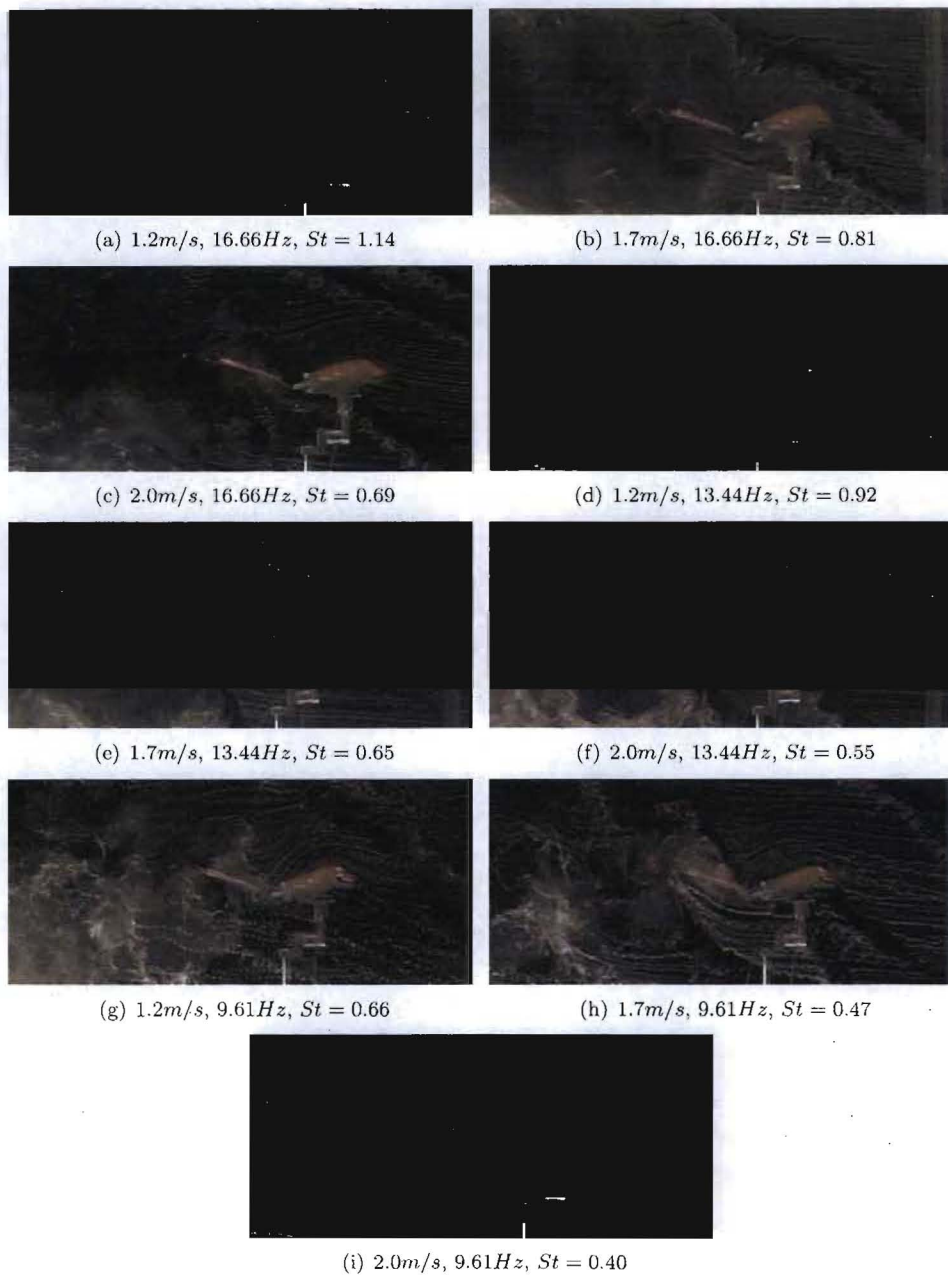
Figure 18. Flow visualization of the wake structures and LEV at an angle of attack of 0°

American Institute of Aeronautics and Astronautics

(a) $1.2m/s$, $16.66Hz$, $St = 0.88$

(b) $1.7m/s$, $16.66Hz$, $St = 0.62$

(c) $2.0m/s$, $16.66Hz$, $St = 0.53$

(d) $1.2m/s$, $13.44Hz$, $St = 0.71$

(e) $1.7m/s$, $13.44Hz$, $St = 0.50$

(f) $2.0m/s$, $13.44Hz$, $St = 0.43$

(g) $1.2m/s$, $9.61Hz$, $St = 0.51$

(h) $1.7m/s$, $9.61Hz$, $St = 0.36$

(i) $2.0m/s$, $9.61Hz$, $St = 0.31$
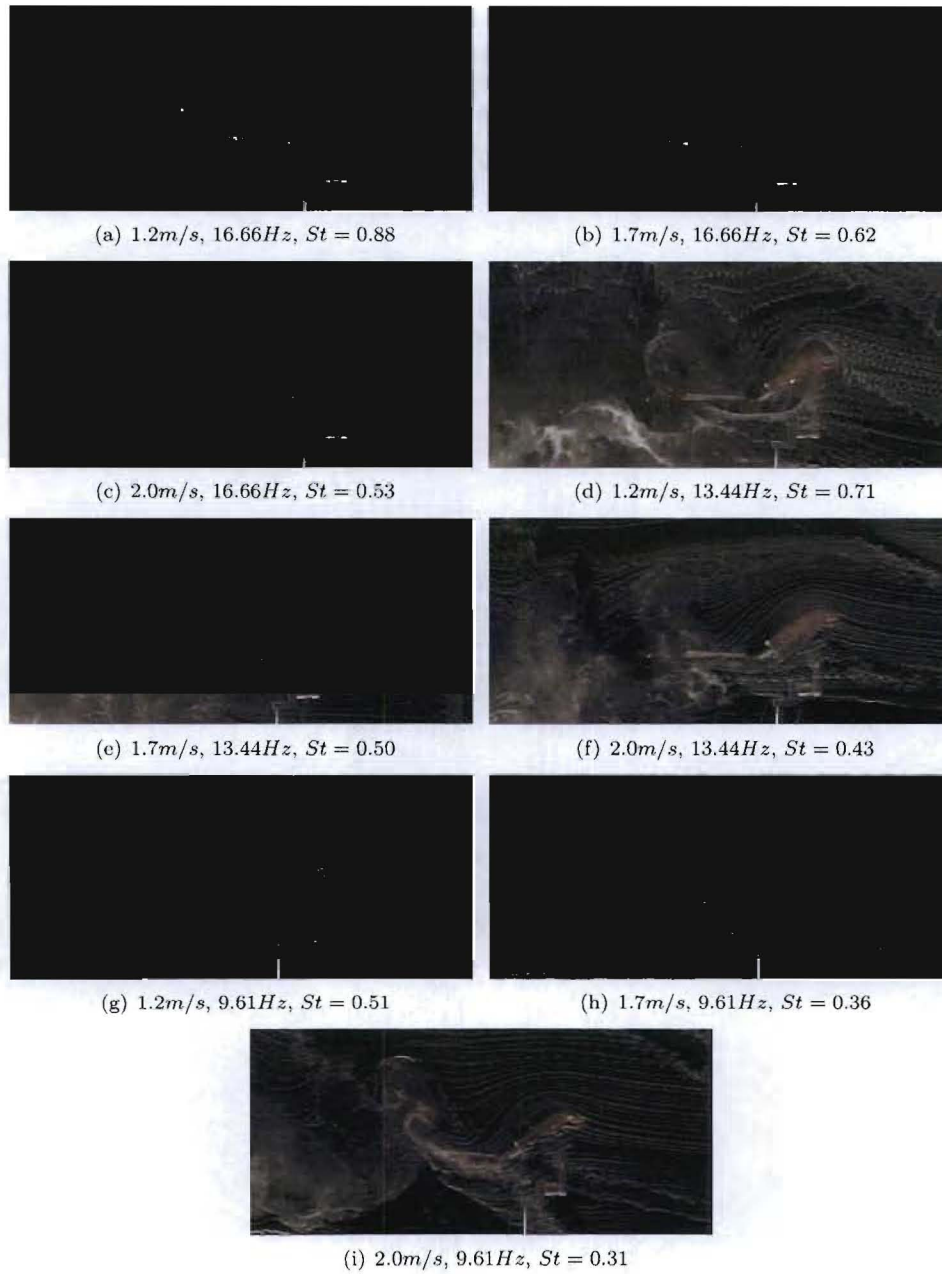
Figure 19. Flow visualization of the wake structures and LEV at an angle of attack of 20°

American Institute of Aeronautics and Astronautics

(a) First frame

(b) Second frame

Figure 20. Images used to determine the trajectories of two fragments of smoke. The smoke fragment traveling over the wing can be seen at two different positions (marked by red squares). The red circle corresponds to the smoke fragment with a speed of 1.7 m/s.
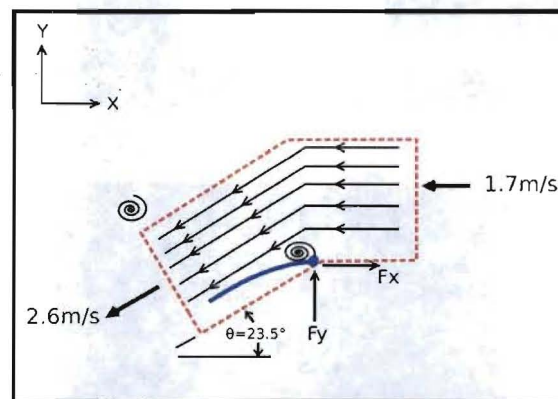

Figure 21. Schematic illustrating the strong momentum ejection during the downstroke. The magnitude of the velocity field above the wing was approximated by visual examination of smoke visualization videos. The blue arc represents the wing of the ornithopter at the end of the downstroke

American Institute of Aeronautics and Astronautics

the ornithopter are very similar to the ones observed by Taylor *et al.*[3] at the same Strouhal number and a similar free-stream velocity and angle of attack (1.5 m/s and 15° respectively). The motions of the wings in both the present experiment and Taylor *et al.*'s experiment are both categorized as root flapping, and they generate a mushroom-shaped wake structure that appears independent of wing flexibility.

According to Taylor *et al.*,[3] at Strouhal numbers greater than 0.45, an energetically inefficient flapping mode is reached. This inefficiency is explained as a consequence of the collision of the wing in upstroke, with shed vorticity at the end of the downstroke. Now, the current ornithopter's free-flight Strouhal number is measured to be 0.8; Hence, it can be expected that the free-flight is rather inefficient based on Taylor *et al.*'s argument. To verify this, the power input into the ornithopter was measured and compared to the work done against the drag. The efficiency (η) of the ornithopter is calculated as:

$$\eta = \frac{T\overline{U}}{VI},$$ (8)

where T is the thrust measured with the force sensor, $\overline{U}$ is the incoming mean flow speed, V is the drive voltage and I is the drive current. The efficiency for this ornithopter was calculated to be about 8% based on measurements of the input power and drag forces. While this low efficiency is consistent with Taylor *et al.*'s argument based on Strouhal numbers, evidence for the collision of the wing with the shed vortices were not observed in the smoke flow visualizations.
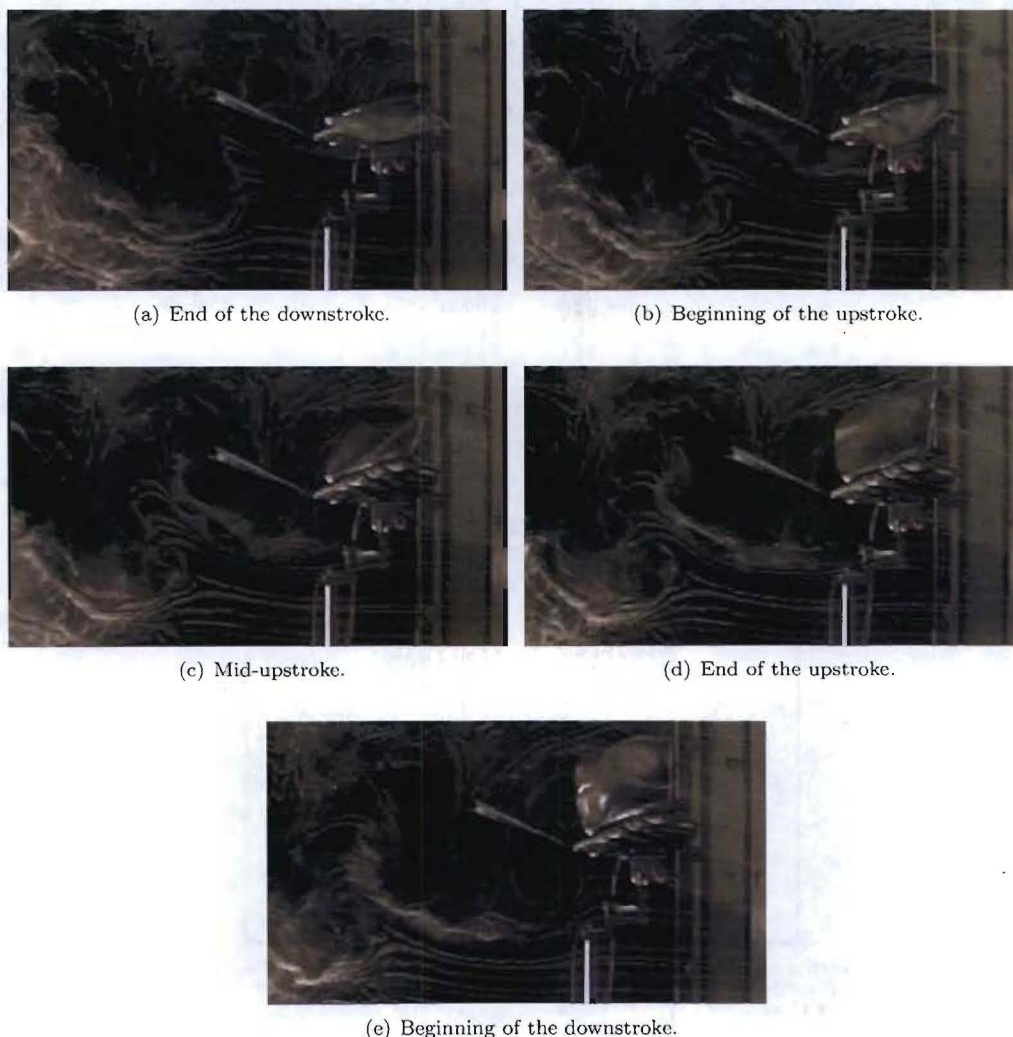

(a) End of the downstroke.

(b) Beginning of the upstroke.

(c) Mid-upstroke.

(d) End of the upstroke.

(e) Beginning of the downstroke.

Figure 22. Flow visualization sequence at $St = 0.46$ **and** $Re = 6,853$

(a) downstroke

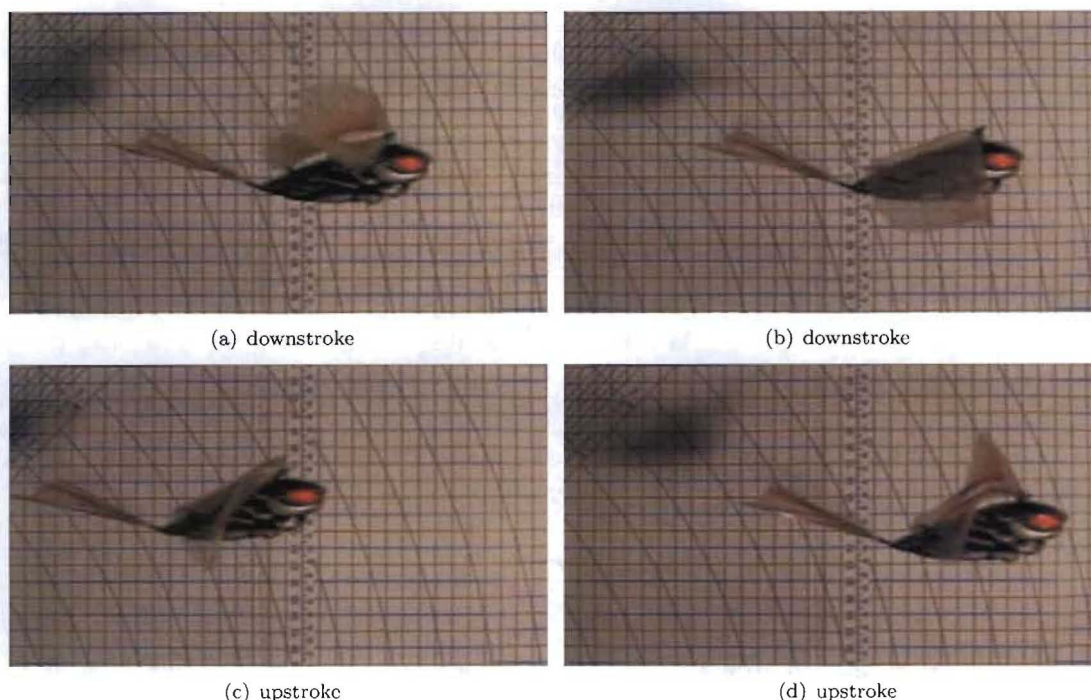(b) downstroke

(c) upstroke

(d) upstroke

Figure 23. Wing deformation during the upstroke and downstroke at $St = 0.8$ and $Re = 8,322$

IV. Conclusion

The aerodynamics of a model ornithopter was investigated by measuring the lift and thrust forces using a six-axis load cell and Particle Image Velocimetry (PIV) techniques. Smoke flow visualization and high speed photography were used to observe the wake flow structures generated by the ornithopter to understand its aerodynamic efficiency.

Force sensor measurements performed at a range of mean velocities, flapping frequencies and angles of attack were used to parametrize the variation of the net lift and thrust forces generated by the flapping wings. The measured lift forces at operating parameters matching the ornithopter's free flight were comparable to the weight of the model. It was also observed that an increase in flapping frequency resulted in an increase in lift force even at high angles of attack. Although this may seem advantageous, this increase in lift at high angles of attack was accompanied by a corresponding loss of thrust. It was found that the lift forces were most sensitive to changes in the angle of attack for small angles of attack while the thrust forces were most sensitive at higher angles of attack. Thus, at shallow angles of steady flight, sudden changes of the angle of attack (caused by a weak gust or turbulent flow, for example) is expected to cause a loss of lift with negligible influence on the thrust.

PIV measurements along the wingspan were used to perform a momentum balance analysis that revealed the distribution of the aerodynamic forces along the wing span. It was clearly seen that for all the cases, the midsection and the wing-root section are the most effective in generating lift and thrust forces. Integration of the thrust and lift distributions along the wing yielded total aerodynamic forces that are in reasonable agreement with the load cell measurements. Deviations of 2% and 20% for the thrust and lift forces were observed between the load-cell and PIV measurements, respectively. These deviations are potentially caused by three-dimensional effects, unsteadiness of the flow, forces generated by other parts of the the ornithopter and the limited number of spanwise measurement planes used in the present study.

Flow visualization for several cases revealed the presence of Leading Edge Vortices (LEV) during the upstroke and downstroke. During the downstroke, a significant downwash was observed for all the cases resulting in strong lift forces. On the contrary, the wing deformation and a positive angle of attack caused a much smaller upward momentum ejection during the upstroke. Thus, flow visualizations clearly showed a larger downward momentum flux during the downstroke when compared to the upstroke, resulting in a net positive lift force that allows the ornithopter to fly.

American Institute of Aeronautics and Astronautics

A visual analysis of high-speed movies during the downstroke revealed a significant change in the magnitude of the flow velocity above the wing. Mushroom-shaped wake structures characteristic of root flapping motion were clearly seen for various Strouhal numbers. These wake structures consisted of shed LEVs and a vortex tube associated with each wing, whose axis of rotation was approximately parallel to the streamwise-wall normal plane. A calculated efficiency of about 8% for the flight parameters of the ornithopter indicate that the wake structures generated by the model correspond to an energetically inefficient mode, consistent with the arguments of Taylor et al.[3] based on the flight Strouhal number. However, no collisions between the shed vortices and the wing plane was observed during the present experiments, providing a possible exception to the mechanism presented in Taylor et al. to explain inefficient flapping flight.

Acknowledgments

References

[1]Kim, D.-K., Han, J.-H., and Kwon. K.-J., "Wind tunnel tests for a flapping wing model with a changeable camber using macro-fiber composite actuators," *Smart Materials and Structures*, Vol. 18, 2009, pp. 1-8.

[2]Godoy-Diana, R., Aider, J.-L., and Wesfreid, J. E., "Transitions in the wake of a flapping foil," *Physical Review E*, Vol. 77, No. 016308, 2008, pp. 1–5.

[3]Taylor, G. K., Nudds, R. L., and Thomas, A. L. R., "Flying and swimming animals cruise at a Strouhal number tuned for high power efficiency," *NATURE*, Vol. 425, 2003, pp. 707–711.

[4]Heathcote, S. and Gursul, I., "Flexible Flapping Airfoil Propulsion at Low Reynolds Numbers," *43rd AIAA Aerospace Sciences Meeting and Exhibit, Reno, NV, January 10-13*, 2005.

[5]Epps, B. P., y Alvarado, P. V., Youcef-Toumi, K., and Techet, A. H., "Swimming performance of a biomimetic compliant fish-like robot," *Experiments in Fluids*, Vol. 47, 2009, pp. 927–939.

[6]Vest, M. S. and Katz, J., "Aerodynamic Study of a Flapping-Wing Micro-UAV," *37th AIAA Aerospace Sciences Meeting and Exhibit, Reno, NV, January 11-14*, 1999.

[7]Lin, C.-S., Hwu, C., and Young, W.-B., "The thrust and lift of an ornithopter's membrane wings with simple flapping motion," *Aerospace Science and Technology*, Vol. 10, 2006, pp. 111–119.

[8]Spedding, G. R., Rosén, M. and Hedenström, A., "A family of vortex wakes generated by a thrush nightingale in free flight in a wind tunnel over its entire natural range of flight speeds," *The Journal of Experimental Biology*, Vol. 206, 2003, pp. 2313–2344.

[9]Raffel, M., Willert, C., and Kompenhans, J., *Particle Image Velocimetry, A Practical Guide*, Springer, 1998.